A Bayesian Approach to Triaxial Strain Tomography from High-energy X-ray Diffraction

J.N. Hendriks[a], C.M. Wensrich[a], A. Wills[a]

[a]*School of Engineering, The University of Newcastle, Callaghan NSW 2308, Australia*

Abstract

Diffraction of high-energy X-rays produced at synchrotron sources can provide rapid strain measurements, with high spatial resolution, and good penetrating power. With an uncollimated diffracted beam, through thickness averages of strain can be measured using this technique. This poses an associated rich tomography problem. This paper proposes a Gaussian process (GP) model for three-dimensional strain fields satisfying equilibrium and an accompanying algorithm for tomographic reconstruction of strain fields from high-energy x-ray diffraction. This method can achieve triaxial strain tomography in three-dimensions using only a single axis of rotation. The method builds upon recent work where the GP approach was used to reconstruct two-dimensional strain fields from neutron based measurements. A demonstration is provided from simulated data, showing the method is capable of rejecting realistic levels of Gaussian noise.

Keywords: Residual strain; X-ray tomography; Gaussian Processes

1. Introduction

Diffraction of X-rays and neutrons allow the study of mechanical stress and strain within crystalline solids [7, 10, 3, 2]. These techniques revolve around Bragg's law; $\lambda = 2d \sin \theta$, whereby variations in the lattice spacing d, due to elastic strain can be observed by changes in the scattering angle, θ, of the diffracted radiation with wavelength λ. These variations are related to the average elastic strain within the scattering volume according to

$$\langle \epsilon \rangle = \frac{d - d_0}{d_0}, \qquad (1)$$

where d_0 is the lattice spacing in a strain free sample. Both neutron and conventional X-ray diffraction have limitations; lab-based x-rays sample only a shallow surface layer (typically a few microns), while the characteristic low intensities of neutrons gives rise to long acquisition times and spatial resolutions of 1mm or larger.

Modern X-ray synchrotron sources can provide very intense narrow beams of highly penetrating X-ray photons [15]. These high-energy X-rays can provide strain measurements with beam spot sizes as small as 1μm and can have path lengths of many centimetres even in steel.

A particular feature of high energy X-rays is that the scattering angle is typically small $2\theta < 15°$ [15]. This has two implications for the study of strain fields: firstly,

that the normal component of strain measured is almost perpendicular to the incident beam; at an angle of $90° - \theta$; secondly, the gauge volume is elongated in the direction of the incident beam (typically by a factor of 10 or more).

The ability to select small beam cross-sections allows strain profiles [1] or two dimensional strain maps [15] to be readily obtained in the plane perpendicular to the incident beam (see Figure 1 for the measurement geometry). However, the resolution along the incident beam is degraded by a factor of 10 or more due to the elongation of the scattering volume. This does not always present a problem, for example in Croft et al. [1] the through thickness strain variation in the direction of the incident beam was known to be small, and averaging in this direction provided a good measure of of strain.

To overcome these limitations, a different approach is presented in [8] and [9] where determining the strain field is considered a rich tomography problem from a series of through thickness measurements. In this setting, the goal is to reconstruct the higher order (two- or three-dimensional) distribution of unknown strain from a set of lower dimension (one- or two-dimensional) profiles. In [8], the axisymmetric strain within a quenched cylinder was reconstructed, providing an initial demonstration of this conceptual approach. This approach was extended in [9], where reconstruction of the longitudinal

strain within a zirconia dental prostheses was achieved by posing the problem in a form suitable for conventional computed tomography algorithms. In this experiment, the sample was rotated about a single axis while through-thickness averages of the out-of-plane normal strain were recorded. The resulting scalar tomography problem was then solved using conventional back-projection techniques.

Importantly, [9] demonstrates how, in-principle, full three-dimensional strain field tomography can be done as a series of 'regular' tomography problems. Here, each regular tomography involves rotating the sample about a single axis and reconstructing the component of strain in the direction of the axis of rotation. By performing six of these experiments about different axes of rotation the full triaxial strain field could be determined.

In this paper we show how, with the addition of equilibrium constraints, this can be done using single axis tomography. Recent work in related fields has demonstrated the use of Gaussian processes (GPs) to model and reconstruct two-dimensional strain fields from time-of-flight neutron transmission measurements [6, 4] and neutron diffraction measurements [5].

1.1. Contribution

This paper makes the following contributions:

1. A Gaussian process model for triaxial elastic strain fields in three-dimensions. This is a non-trivial extension of the model presented in Jidling et al. [6] which was restricted to biaxial strain fields in two dimensions under the assumption of plane stress or plane strain.

2. A method for applying this model to reconstruct the strain field from high-energy X-ray strain measurements. This allows a triaxial strain field to be reconstructed using single axis tomography. This could not be achieved using existing methods.

2. High Energy X-ray Strain Measurement

This section provides a brief summary of strain measurement using high energy x-ray diffraction. This process is not the primary focus of this work, however the summary provides details pertinent to model the relationship between the measurements and the strain field. A more detailed description can be found in [15] and details of geometric corrections required due to rotating the sample causing changes in the sample to detector distance are describe in [9]. The summary is as follows.

The incident beam, with direction $\hat{\mathbf{n}}$, is diffracted within the sample, according to Bragg's law, at an angle of 2θ forming a shallow cone. The intensity of the diffracted beam is recorded at a detector, with the peak intensity's forming a ring; known as a Debye-Scherrer ring, see Figure 1. Due to the small diffraction angles the distance to the detector, D, is much greater than nominal sample dimensions.

A Bragg peak can be fit to a segment of the Debye-Scherrer ring providing a measurement of the average normal strain in the direction κ of the form (1); with a $10°$ being suitable for strain measurements [9]. Multiple segments can be analysed from each Debye-Scherrer ring to give measurements of the normal strain in different directions.

In this work, we consider the diffracted beam to be left uncollimated—which aligns with the work in Korsunsky et al. [9], and the incident beam to be collimated to give a spot size of $h \times h$. This measurement geometry is shown in Figure 2 and gives the scattering volume's length as the path length through the sample, L. Given that spot sizes as small as 1μm are achievable and that typical path lengths can be several orders of magnitude larger, it is reasonable to model the measurements by the line integral

$$I_\epsilon = \frac{1}{L} \int\limits_0^L \hat{\boldsymbol{\kappa}}^\mathsf{T} \boldsymbol{\epsilon}(\mathbf{p} + \hat{\mathbf{n}}s)\hat{\boldsymbol{\kappa}} \, \mathrm{d}s + e, \qquad (2)$$

where $e \sim \mathcal{N}(0, \sigma_n^2)$, $\boldsymbol{\epsilon}(\mathbf{x})$ is the strain tensor field inside the sample and $\mathbf{p}$ is the initial intersection between the beam and the sample.
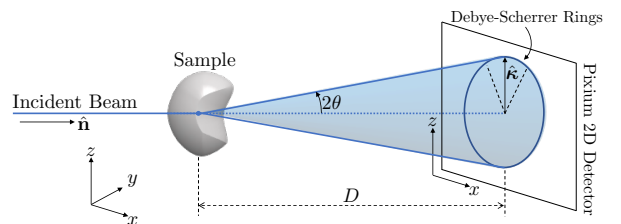

Figure 1: Measurement geometry. The incident beam, with direction $\hat{\mathbf{n}}$, is diffracted by the sample at an angle of 2θ forming a shallow cone. The peak intensities of this cone, known as a Debye-Scherrer ring, are recorded by a detector at distance D. A segment of this ring can be analysed to provide a measurement of normal strain in the direction $\hat{\boldsymbol{\kappa}}$. Figure is not to scale.

3. 3D Strain field Reconstruction

In this work, the strain field is reconstructed using the framework of Bayesian inference. The strain field is
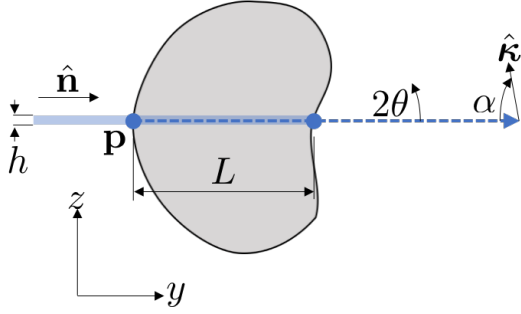
Figure 2: Scattering volume geometry. Shown is a cross section of the sample, and the incident and diffracted beams in the plane defined by $\hat{\mathbf{n}}$ and $\hat{\boldsymbol{\kappa}}$. The incident beam spot size $h \times h$, L is the through thickness length of the scattering volume, $\alpha = 90 - \theta$ is the angle from the incident beam to the measured normal strain direction, and $\mathbf{p}$ is the initial intersection of the beam and the sample. Figure not to scale.

modelled as having a probability distribution, this does not mean that the strain field is random, instead it represents our uncertainty in its values. A *prior* probability distribution is assigned to the strain field, $p(\boldsymbol{\epsilon})$, that represents any knowledge we have before the inclusion of measurements, y. This distribution is then updated by the inclusion of measurements, which are assigned a *likelihood* $p(y|\boldsymbol{\epsilon})$, using Bayes' rule to give a *posterior* distribution of the strain:

$$p(\boldsymbol{\epsilon}|y) = \frac{p(y|\boldsymbol{\epsilon})p(\boldsymbol{\epsilon})}{p(y)}. \tag{3}$$

As the strain field must satisfy equilibrium, the prior distribution should incorporate this knowledge. In two dimensions this can be achieved by modelling the Airy's stress function by a Gaussian process (GP) from which the two-dimensional strain field can be defined under an assumption of plane stress or plane strain [6]. This method was successfully used to reconstruct two-dimensional strain fields from neutron transmission measurements [6, 4] and neutron diffraction measurements [5].

The following sections present a generalisation of this procedure to three-dimensions and application to reconstructing the strain field from from high energy x-ray diffraction measurements. A brief overview of GPs is provided in Section 3.1. A Gaussian process prior suitable for modelling three-dimensional strain fields is designed in Section 3.2. A likelihood model for high energy x-ray strain measurements is then defined, allowing the strain field to be reconstructed; Section 3.3. The method presented assumes that the material is isotropic and free of texture.

3.1. Gaussian Process

This section gives a brief description of GPs, for a more detailed description see Rasmussen and Williams [11]. A GP is a stochastic process suitable for modelling spatially correlated functions and can be viewed as a distribution over functions;

$$f(\mathbf{x}) \sim \mathcal{GP}\left(m(\mathbf{x}), k(\mathbf{x}, \mathbf{x}')\right), \tag{4}$$

where $m(\mathbf{x}) = \mathbb{E}\left[f(\mathbf{x})\right]$ is the mean function and $k(\mathbf{x}, \mathbf{x}') = \mathbb{E}\left[(m(\mathbf{x}) - f(\mathbf{x}))(m(\mathbf{x}) - f(\mathbf{x}))^{\mathsf{T}}\right]$ is the covariance function. The choice of covariance function governs the characteristics of the functions in this distribution—such as their smoothness. Many choices exist for the covariance function [11], and a good summary is available in Rasmussen and Williams [11].

A Gaussian process is a generalisation of a multivariate Gaussian in the sense that function values sampled at a finite number of inputs $\mathbf{x}_1, \ldots, \mathbf{x}_N$ are Gaussian distributed;

$$\begin{bmatrix} f(\mathbf{x}_1) \\ \vdots \\ f(\mathbf{x}_N) \end{bmatrix} \sim \mathcal{N}(\boldsymbol{\mu}, \mathbf{K}) \quad \text{where} \quad \boldsymbol{\mu} = \begin{bmatrix} m(\mathbf{x}_1) \\ \vdots \\ m(\mathbf{x}_N) \end{bmatrix}, \tag{5a}$$

and

$$\mathbf{K} = \begin{bmatrix} k(\mathbf{x}_1, \mathbf{x}_1) & \cdots & k(\mathbf{x}_1, \mathbf{x}_N) \\ \vdots & \ddots & \vdots \\ k(\mathbf{x}_N, \mathbf{x}_1) & \cdots & k(\mathbf{x}_N, \mathbf{x}_N) \end{bmatrix}. \tag{5b}$$

If a GP prior is used and the measurement likelihood is Gaussian then posterior distribution given by Bayes' rule has a closed form and can be computed using standard Gaussian conditioning.

3.2. Three-dimensional Strain Field GP

Here, we design a GP prior for strain in three-dimensions that intrinsically satisfies equilibrium. The strain field is defined as the symmetric tensor

$$\boldsymbol{\epsilon}(\mathbf{x}) = \begin{bmatrix} \epsilon_{xx}(\mathbf{x}) & \epsilon_{xy}(\mathbf{x}) & \epsilon_{xz}(\mathbf{x}) \\ \epsilon_{xy}(\mathbf{x}) & \epsilon_{yy}(\mathbf{x}) & \epsilon_{yz}(\mathbf{x}) \\ \epsilon_{xz}(\mathbf{x}) & \epsilon_{yz}(\mathbf{x}) & \epsilon_{zz}(\mathbf{x}) \end{bmatrix}, \tag{6}$$

where $\mathbf{x} = [x \; y \; z]^{\mathsf{T}}$ are the spatial coordinates.

This GP will be of the form

$$\bar{\boldsymbol{\epsilon}} \sim \mathcal{GP}\left(\mathbf{0}, \mathbf{K}_{\epsilon}(\mathbf{x}, \mathbf{x}')\right), \tag{7}$$

where $\bar{\boldsymbol{\epsilon}}$ is a vector of the 6 unique components of the strain field. Here, the covariance function for the strain field, $\mathbf{K}_{\epsilon}(\mathbf{x}, \mathbf{x}')$ will be designed to ensure that all strain fields belonging to this GP satisfy equilibrium. This is

done by specifying a GP prior for a set of potentials known as the Beltrami stress functions. Having done this, a GP prior for the strain field can be derived using the equilibrium equations and Hooke's law. The details of this derivation are as follows.

The Beltrami stress functions allow a complete solution to the equilibrium equations in three-dimensions to be written as [12]

$$\sigma(\mathbf{x}) = \nabla \times \Phi(\mathbf{x}) \times \nabla, \qquad (8)$$

where $\nabla = \begin{bmatrix} \frac{\partial}{\partial x} & \frac{\partial}{\partial y} & \frac{\partial}{\partial z} \end{bmatrix}^{\mathsf{T}}$ and $\sigma(x, y, z)$ is the symmetric stress tensor;

$$\sigma(x, y, z) = \begin{bmatrix} \sigma_{xx}(\mathbf{x}) & \sigma_{xy}(\mathbf{x}) & \sigma_{xz}(\mathbf{x}) \\ \sigma_{xy}(\mathbf{x}) & \sigma_{yy}(\mathbf{x}) & \sigma_{yz}(\mathbf{x}) \\ \sigma_{xz}(\mathbf{x}) & \sigma_{yz}(\mathbf{x}) & \sigma_{zz}(\mathbf{x}) \end{bmatrix}, \qquad (9)$$

and $\Phi(x, y, z)$ is the Beltrami stress tensor consisting of six unique scalar potential fields;

$$\Phi(\mathbf{x}) = \begin{bmatrix} \Phi_1(\mathbf{x}) & \Phi_4(\mathbf{x}) & \Phi_5(\mathbf{x}) \\ \Phi_4(\mathbf{x}) & \Phi_2(\mathbf{x}) & \Phi_6(\mathbf{x}) \\ \Phi_5(\mathbf{x}) & \Phi_6(\mathbf{x}) & \Phi_3(\mathbf{x}) \end{bmatrix}. \qquad (10)$$

To improve readability we introduce the following vectorised notation;

$$\bar{\Phi} = \begin{bmatrix} \Phi_1 \\ \Phi_2 \\ \Phi_3 \\ \Phi_4 \\ \Phi_5 \\ \Phi_6 \end{bmatrix}, \quad \bar{\sigma} = \begin{bmatrix} \sigma_{xx} \\ \sigma_{yy} \\ \sigma_{zz} \\ \sigma_{xy} \\ \sigma_{xz} \\ \sigma_{zz} \end{bmatrix}, \quad \bar{\epsilon} = \begin{bmatrix} \epsilon_{xx} \\ \epsilon_{yy} \\ \epsilon_{zz} \\ \epsilon_{xy} \\ \epsilon_{xz} \\ \epsilon_{yz} \end{bmatrix}, \qquad (11)$$

where the spatial coordinates $\mathbf{x}$, are omitted for brevity. Using this notation we can write Hooke's law which relates the stress and strain fields as

$$\begin{bmatrix} \epsilon_{xx} \\ \epsilon_{yy} \\ \epsilon_{zz} \\ \epsilon_{xy} \\ \epsilon_{xz} \\ \epsilon_{yz} \end{bmatrix} = \underbrace{\begin{bmatrix} 1 & -\nu & -\nu & 0 & 0 & 0 \\ -\nu & 1 & -\nu & 0 & 0 & 0 \\ -\nu & -\nu & 1 & 0 & 0 & 0 \\ 0 & 0 & 0 & 1+\nu & 0 & 0 \\ 0 & 0 & 0 & 0 & 1+\nu & 0 \\ 0 & 0 & 0 & 0 & 0 & 1+\nu \end{bmatrix}}_{\mathbf{H}} \begin{bmatrix} \sigma_{xx} \\ \sigma_{yy} \\ \sigma_{zz} \\ \sigma_{xy} \\ \sigma_{xz} \\ \sigma_{zz} \end{bmatrix}, \qquad (12)$$

where $\mathbf{H}$ is the compliance matrix for isotropic materials. Finally, we can write the mapping from the Beltrami stress functions to the strain field in this vectorised form as

$$\bar{\epsilon} = \mathbf{H}\mathcal{B}^{\mathbf{x}}\bar{\Phi}, \qquad (13)$$

where

$$\mathcal{B}^{\mathbf{x}} = \begin{bmatrix} 0 & \frac{\partial^2}{\partial z^2} & \frac{\partial^2}{\partial y^2} & 0 & 0 & -2\frac{\partial^2}{\partial y \partial z} \\ \frac{\partial^2}{\partial z^2} & 0 & \frac{\partial^2}{\partial x^2} & 0 & -2\frac{\partial^2}{\partial x \partial z} & 0 \\ \frac{\partial^2}{\partial y^2} & \frac{\partial^2}{\partial x^2} & 0 & -2\frac{\partial^2}{\partial x \partial y} & 0 & 0 \\ 0 & 0 & -\frac{\partial^2}{\partial x \partial y} & -\frac{\partial^2}{\partial z^2} & \frac{\partial^2}{\partial y \partial z} & \frac{\partial^2}{\partial x \partial z} \\ -\frac{\partial^2}{\partial y \partial z} & 0 & 0 & \frac{\partial^2}{\partial x \partial z} & \frac{\partial^2}{\partial x \partial y} & -\frac{\partial^2}{\partial x^2} \\ 0 & -\frac{\partial^2}{\partial x \partial z} & 0 & \frac{\partial^2}{\partial y \partial z} & -\frac{\partial^2}{\partial y^2} & \frac{\partial^2}{\partial x \partial y} \end{bmatrix}, \qquad (14)$$

and the superscript is used to denote the set of spatial coordinates on which the operator acts.

As this mapping is linear it can be used to define a GP prior on the strain function [14, 11, 6]. First, a GP prior is defined for $\bar{\Phi}$ where each Φ_i is assumed to be independent;

$$\bar{\Phi} \sim \mathcal{GP}\left(\underbrace{\begin{bmatrix} m_1(\mathbf{x}) \\ m_2(\mathbf{x}) \\ m_3(\mathbf{x}) \\ m_4(\mathbf{x}) \\ m_5(\mathbf{x}) \\ m_6(\mathbf{x}) \end{bmatrix}}_{\mathbf{m}_\Phi(\mathbf{x})}, \underbrace{\begin{bmatrix} K_1 & 0 & 0 & 0 & 0 & 0 \\ 0 & K_2 & 0 & 0 & 0 & 0 \\ 0 & 0 & K_3 & 0 & 0 & 0 \\ 0 & 0 & 0 & K_4 & 0 & 0 \\ 0 & 0 & 0 & 0 & K_5 & 0 \\ 0 & 0 & 0 & 0 & 0 & K_6 \end{bmatrix}}_{\mathbf{K}_\Phi(\mathbf{x},\mathbf{x}')} \right). \qquad (15)$$

The mapping (3.2) is applied to give a GP prior for the strain field that will ensure that any estimated strain field satisfies equilibrium;

$$\bar{\epsilon} \sim \mathcal{GP}\left(\mathbf{H}\mathcal{B}^{\mathbf{x}}\mathbf{m}_\Phi, \mathbf{H}\mathcal{B}^{\mathbf{x}}\mathbf{K}_\Phi\mathcal{B}^{\mathbf{x}'\,\mathsf{T}}\mathbf{H}^{\mathsf{T}} \right) = \mathcal{GP}\left(\mathbf{0}, \mathbf{K}_\epsilon \right) \quad (16)$$

where, without loss of generality [11], we chose the prior mean functions as zero.

3.3. Reconstruction from X-ray Strain Measurements

Here, we define the likelihood of the x-ray strain measurements $p(I_\epsilon | \epsilon)$. In vector form we can write the measurement model as

$$I_\epsilon(\eta) = \frac{1}{L} \int_0^L \bar{\kappa}\bar{\epsilon}(\mathbf{p} + \hat{\mathbf{n}}s)\,\mathrm{d}s + e \qquad (17)$$

$$I_\epsilon(\eta) = \mathcal{L}^{\mathbf{x}}(\eta)\bar{\epsilon}(\mathbf{x}) + e$$

where $\bar{\kappa} = \begin{bmatrix} \kappa_x^2 & \kappa_y^2 & \kappa_z^2 & 2\kappa_x\kappa_y & 2\kappa_x\kappa_z & 2\kappa_y\kappa_z \end{bmatrix}$, $\eta = \{\kappa, \hat{\mathbf{n}}, \mathbf{p}, L\}$, $e \sim \mathcal{N}(0, \sigma_n^2)$, and $\mathcal{L}^{\mathbf{x}}(\eta)$ is a considered an operator that maps from the strain function $\bar{\epsilon}(\mathbf{x})$ into the measurements $I_\epsilon(\eta)$. As this operator is linear, the joint distribution of the strain field at user specified location of interest, $\bar{\epsilon}_* = \bar{\epsilon}(\mathbf{x}_*)$, and the measurements $\mathbf{I}_\epsilon = \begin{bmatrix} I_\epsilon(\eta_1) & \cdots & I_\epsilon(\eta_n) \end{bmatrix}^{\mathsf{T}}$ is Gaussian [14, 11, 6];

4

$$\begin{bmatrix} \mathbf{I}_\epsilon \\ \bar{\boldsymbol{\epsilon}}_* \end{bmatrix} = \mathcal{N}\left(\begin{bmatrix} \mathbf{0} \\ \mathbf{0} \end{bmatrix}, \begin{bmatrix} \mathbf{K}_I + \sigma_n^2\mathbf{I} & \mathbf{K}_*^\mathsf{T} \\ \mathbf{K}_* & \mathbf{K}_\epsilon \end{bmatrix} \right), \qquad (18)$$

where $\mathbf{K}_*$ is the cross covariance between the strains and the measurements and $\mathbf{K}_I$ is the covariance of the measurements.

The cross covariance between the strain $\bar{\boldsymbol{\epsilon}}_*$ and a measurement $I_\epsilon(\boldsymbol{\eta}_i)$ is given by a single application of (17) to the strain fields covariance function;

$$\begin{aligned} (\mathbf{K}_*)_i &= \mathbf{K}_\epsilon \mathcal{L}^{\mathbf{x}'}(\boldsymbol{\eta}_i)^\mathsf{T} \\ &= \frac{1}{L_i} \int_0^{L_i} \mathbf{K}_\epsilon(\mathbf{x}_*, \mathbf{p}_i + \hat{\mathbf{n}}_i s') \bar{\boldsymbol{\kappa}}_i^\mathsf{T}\, \mathrm{d}s' \end{aligned} \qquad (19)$$

and the covariance between each pair of measurements, $I_\epsilon(\boldsymbol{\eta}_i)$ and $I_\epsilon(\boldsymbol{\eta}_j)$ is similarly given by

$$\begin{aligned} (\mathbf{K}_I)_{ij} &= \mathcal{L}^{\mathbf{x}}(\boldsymbol{\eta}_i) \mathbf{K}_\epsilon \mathcal{L}^{\mathbf{x}'}(\boldsymbol{\eta}_j)^\mathsf{T} \\ &= \frac{1}{L_i L_j} \int_0^{L_i}\!\!\int_0^{L_j} \bar{\boldsymbol{\kappa}}_i \mathbf{K}_\epsilon(\mathbf{p}_i + \hat{\mathbf{n}}_i s, \mathbf{p}_j + \hat{\mathbf{n}}_j s') \bar{\boldsymbol{\kappa}}_j^\mathsf{T}\, \mathrm{d}s'\mathrm{d}s \end{aligned}$$
$$(20)$$

The posterior distribution of the strain $\bar{\boldsymbol{\epsilon}}$ conditioned on the measurements $\mathbf{I}_\epsilon$ is

$$\bar{\boldsymbol{\epsilon}}_* \sim \mathcal{N}(\boldsymbol{\mu}_{\bar{\epsilon}|\mathbf{I}_\epsilon}, \mathbf{K}_{\epsilon_*|\mathbf{I}_\epsilon}) \qquad (21)$$

where

$$\begin{aligned} \boldsymbol{\mu}_{\bar{\epsilon}|\mathbf{I}_\epsilon} &= \mathbf{K}_*(\mathbf{K}_I + \sigma_n^2\mathbf{I})^{-1}\mathbf{I}_\epsilon \\ \mathbf{K}_{\epsilon_*|\mathbf{I}_\epsilon} &= \mathbf{K}_\epsilon(\mathbf{x}_*, \mathbf{x}_*) - \mathbf{K}_*(\mathbf{K}_I + \sigma_n^2\mathbf{I})^{-1}\mathbf{K}_*^\mathsf{T} \end{aligned} \qquad (22)$$

An analytic solution to the double integral is not known. However, computationally expensive numerical integration can be avoided by using an approximation scheme such as the one described in Section 4.1. It is worth noting that the extension to non-convex geometry is straight forward [6].

4. Implementation

Two practical aspects need to be considered when implementing the reconstruction algorithm; computational complexity, and hyperparameter selection.

4.1. Reducing Computation Complexity

The computational complexity of solving Equation (22) is twofold: firstly, the construction of $\mathbf{K}_{II}$ requires the evaluation of a double integral for every unique pair of measurements; secondly, the time required to invert $\mathbf{K}_{II} + \sigma_n^2\mathbf{I}$ scales with $O(N^3)$. X-ray strain tomography problems of the type considered here have a large number of measurements, motivating the use of an approximation scheme. Here, we consider the approximation scheme proposed in [13] which has previously been used for strain estimation [6, 5]. Using this scheme the covariance functions assigned to the Beltrami stress functions, $\mathbf{K}_{\Phi_i}$, can be approximated by a finite series of m basis functions;

$$\begin{aligned} K_i(\mathbf{x}, \mathbf{x}') &\approx \sum_{k=1}^m \phi_{i,k}(\mathbf{x})\Sigma_{pi,kk}\phi_{i,k}(\mathbf{x}') \\ &= \boldsymbol{\phi}_i(\mathbf{x})\Sigma_{pi}\boldsymbol{\phi}_i(\mathbf{x}')^\mathsf{T}, \end{aligned} \qquad (23)$$

where each $\phi_{i,k}(\mathbf{x})$ is a basis function and $\Sigma_{pi,kk}$ is its spectral density;

$$\begin{aligned} \phi_{i,k}(x) &= \frac{1}{L_x L_y L_z} \sin(\lambda_{xk}(x + L_x)) \\ &\qquad \sin(\lambda_{yk}(y + L_y)) \sin(\lambda_{zk}(z + L_z)), \quad (24) \\ \Sigma_{pi,k} &= \int K(\mathbf{r}) \exp(-i\lambda^\mathsf{T}\mathbf{r})\, \mathrm{d}r. \end{aligned}$$

Here, $\mathbf{r} = \mathbf{x} - \mathbf{x}'$, and $\lambda = [\lambda_{xj}\ \lambda_{yj}\ \lambda_{zj}]^\mathsf{T}$. For the squared-exponential covariance function used in Section 5 the spectral density is

$$\Sigma_{pi,kk} = \sigma_f^2(2\pi)^{\frac{3}{2}} l_x l_y l_z \exp\left(-\frac{1}{2}\left(l_x^2\lambda_{xk}^2 + l_y^2\lambda_{yk}^2 + l_z^2\lambda_{zk}^2\right)\right),$$
$$(25)$$

where σ_f, l_x, l_y, and l_z are commonly referred to as hyper-parameters and are discussed in Section 4.2. The parameters L_x, L_y, L_z, and λ are analogous to the frequency and phase of the basis functions.

In this work, they were chosen so that the basis functions spanned a region where their spectral densities were greater than a predefined minimum threshold. This helps to ensure numerical stability while capturing the dominant modes of the reconstruction.

By concatenating the basis functions we can concisely express the approximation for the covariance function $\mathbf{K}_\Phi$;

$$\mathbf{K}_\Phi \approx \boldsymbol{\phi}_\Psi \Sigma_\Psi \boldsymbol{\phi}_\Psi^\mathsf{T},$$
$$\boldsymbol{\phi}_\Psi = \begin{bmatrix} \boldsymbol{\phi}_1 \\ \boldsymbol{\phi}_2 \\ \boldsymbol{\phi}_3 \\ \boldsymbol{\phi}_4 \\ \boldsymbol{\phi}_5 \\ \boldsymbol{\phi}_6 \end{bmatrix}^\mathsf{T}, \quad \Sigma_\Psi = \begin{bmatrix} \Sigma_{p1} & 0 & 0 & 0 & 0 & 0 \\ 0 & \Sigma_{p2} & 0 & 0 & 0 & 0 \\ 0 & 0 & \Sigma_{p3} & 0 & 0 & 0 \\ 0 & 0 & 0 & \Sigma_{p4} & 0 & 0 \\ 0 & 0 & 0 & 0 & \Sigma_{p5} & 0 \\ 0 & 0 & 0 & 0 & 0 & \Sigma_{p6} \end{bmatrix} \quad (26)$$

It is now a straight forward application of the mappings (3.2) and (17) to approximate the covariances required in Section 3 to reconstruct the strain field;

$$\mathbf{K}_\epsilon \approx \boldsymbol{\phi}_\epsilon(\mathbf{x}_*)\Sigma_\Psi\boldsymbol{\phi}_\epsilon(\mathbf{x}_*)^\top$$

$$(\mathbf{K}_*)_i \approx \boldsymbol{\phi}_\epsilon(\mathbf{x}_*)\Sigma_\Psi\boldsymbol{\phi}_\mathbf{I}(\boldsymbol{\eta}_i)^\top \qquad (27a)$$

$$(\mathbf{K}_\mathbf{I})_{ij} \approx \boldsymbol{\phi}_\mathbf{I}(\boldsymbol{\eta}_i)\Sigma_\Psi\boldsymbol{\phi}_\mathbf{I}(\boldsymbol{\eta}_j)^\top$$

where

$$\boldsymbol{\phi}_\epsilon(\mathbf{x}_*) = \mathbf{H}\mathcal{B}^\mathbf{x}\boldsymbol{\phi}_\Phi(\mathbf{x}_*) = \boldsymbol{\phi}_*$$

$$\boldsymbol{\phi}_{I,i}(\boldsymbol{\eta}_i) = \mathcal{L}^\mathbf{x}(\boldsymbol{\eta}_i)\boldsymbol{\phi}_\epsilon(\mathbf{p}_i + \hat{\mathbf{n}}s) = \boldsymbol{\phi}_{I,i} \qquad i = 1,\ldots,N$$
$$(27b)$$

This simplifies the problem to the calculation of $\boldsymbol{\phi}_\epsilon(\mathbf{x}_*)$ and $\boldsymbol{\phi}_{I,i}(\boldsymbol{\eta}_i)$, which are intuitively the basis functions for the strain field and the measurements, respectively, and only require a single application of the mappings. Complete expressions for these basis functions are found in Appendix Appendix A.

The posterior mean and covariance are approximated by

$$\boldsymbol{\mu}_{\epsilon_*|\mathbf{I}} \approx \boldsymbol{\phi}_* \left(\boldsymbol{\phi}_I^\top\sigma_n^{-2}\boldsymbol{\phi}_I + \Sigma_\Psi^{-1}\right)^{-1}\boldsymbol{\phi}_I^\top\sigma_n^{-2}\mathbf{I}_\epsilon$$

$$\mathbf{K}_{\epsilon_*|\mathbf{I}} \approx \boldsymbol{\phi}_* \left(\boldsymbol{\phi}_I^\top\sigma_n^{-2}\boldsymbol{\phi}_I + \Sigma_\Psi^{-1}\right)^{-1}\boldsymbol{\phi}_*^\top$$
$$(28)$$

This avoids forming the covariance matrices, reduces the complexity of the regression to $O(Nm^2)$ and also removes the need for numerical derivatives.

4.2. Hyperparameter Optimisation

The covariance functions, assigned to the potential functions, are characterised by their hyperparameters $\boldsymbol{\theta}$. For example, the squared-exponential covariance function has hyperparameters $\boldsymbol{\theta} = \{\sigma_f, l_x, l_y, l_z\}$; where σ_f encodes our prior uncertainty and the length scales l_x, l_y, and l_z provide an assumption of smoothness. The hyperparmaters are selected by maximising the marginal log likelihood, $\log p(\mathbf{I}_\epsilon|\{\boldsymbol{\eta}_i\}, \boldsymbol{\theta})$;

$$\boldsymbol{\theta}_* = \underset{\boldsymbol{\theta}}{\mathrm{argmax}}\left[-\frac{1}{2}\log\det(\mathbf{K}_{II} + \sigma_n^2\mathbf{I}) - \frac{1}{2}\mathbf{I}_\epsilon^\top(\mathbf{K}_{II} + \sigma_n^2\mathbf{I})^{-1}\mathbf{I}_\epsilon\right],$$
$$(29)$$

where $\mathbf{K}_{II}$ is a function of $\boldsymbol{\theta}$. For the approximation in Section 4.1 $\mathbf{K}_{II}$ is replaced by $\boldsymbol{\phi}_I\Sigma_p\boldsymbol{\phi}_I^\top$, and expressions for the approximate log likelihood and its derivatives can be found in [5] or [6]. The parameters can thereafter be optimised using a gradient-based method, such as the BFGS algorithm in Wright and Nocedal [16].
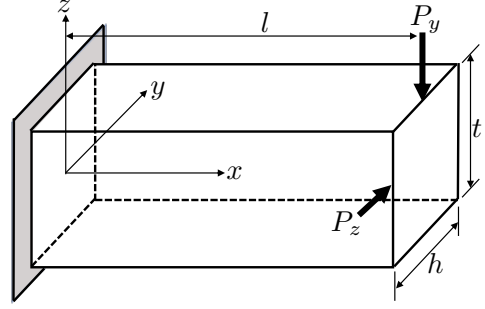

Figure 3: Three-dimensional Cantilever beam geometry and coordinate system with $l = 20$mm, $h = 10$mm, $t = 6$mm, $E = 200$GPa, $P_y = 2$kN, $P_z = 1$kN, $\nu = 0.28$, $I_{yy} = \frac{th^3}{12}$, and $I_{zz} = \frac{t^3h}{12}$. The triaxial strain field is given by a superposition of the Saint-Venant approximation to the strain field in the xy- and yz-planes as per Equation 30.

5. Simulation Demonstration

The method presented is demonstrated on a simulated 3D cantilevered beam example with the strain field given by a superposition of the Saint-Venant approximation to the strain field in the xy- and yz-planes. This is chosen as an appropriate example in the absence of a suitable experimental data set. The strain field is given by

$$\epsilon_{xx}(\mathbf{x}) = \frac{P_y(l-x)y}{EI_{yy}} + \frac{P_z(l-x)z}{EI_{zz}}$$

$$\epsilon_{yy}(\mathbf{x}) = -\nu\frac{P_y(l-x)y}{EI_{yy}} - \nu\frac{P_z(l-x)z}{EI_{zz}}$$

$$\epsilon_{zz}(\mathbf{x}) = -\nu\frac{P_y(l-x)y}{EI_{yy}} - \nu\frac{P_z(l-x)z}{EI_{zz}}$$

$$\epsilon_{xy}(\mathbf{x}) = -(1+\nu)\frac{P_y(\frac{1}{4}h^2 - y^2)}{EI_{yy}} \qquad (30)$$

$$\epsilon_{xz}(\mathbf{x}) = -(1+\nu)\frac{P_z(\frac{1}{4}t^2 - z^2)}{EI_{zz}}$$

$$\epsilon_{yz}(\mathbf{x}) = 0$$

where geometry and loading is defined in Figure 3

Measurements were simulated through these strain fields using Equation (17). The measurement geometry corresponded to rotating the sample about z and for each angle using a 40×40 grid of incident beams. For each incident beam 36 strain directions are measured, corresponding to using $10°$ segments from the Debye-Scherrer rings. The measurements were corrupted by zero-mean Gaussian noise with standard deviation $\sigma_m = 1 \times 10^{-4}$.

A convergence study as the number of rotation angles is increased was run and the results are shown in Figure 4. For each simulation the n_ψ angles were chosen to

be linearly spaced over $\frac{n_\psi}{n_\psi + 1} 180°$. From equation 17 it is clear that two beams with travelling along the same path but with opposite directions provide measurements of almost identical components of the strain field. Therefore, it is not necessary to choose angles spanning 360°.
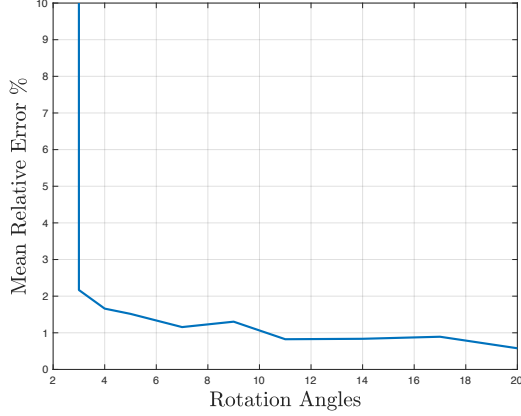

Figure 4: Convergence of the reconstruction in simulation as the number of rotation angles is increase. The mean relative error is shown.

These results indicate that at least three rotation angles are required for an accurate reconstruction. This is true regardless of the number of incident beams used per rotation angle, and intuitively can be explained as each rotation angle the incident beams predominantly provide information about the strains lying in the plane perpendicular to the beams. Hence, three unique sets of these 'in-plane' strains need to be observed to recover the three-dimensional strain field.

The results of reconstructing from the final measurement set generated using 20 rotation angles are shown in Figure 5. The results show the reconstructed effective and hydrostatic strains along two cutting planes, which give a good indication of the overall accuracy of the reconstruction. The effective[1], ϵ_{eff}, and hydrostatic, ϵ_{hyd}, strains are defined as

$$
\epsilon_{\text{hyd}} = \frac{1}{3} \left(\epsilon_{xx} + \epsilon_{yy} + \epsilon_{zz} \right)
$$
$$
\epsilon_{\text{eff}} = \left(\frac{2}{3} \left(\epsilon_{xx} - \epsilon_{\text{hyd}} \right)^2 + \frac{2}{3} \left(\epsilon_{yy} - \epsilon_{\text{hyd}} \right)^2 + \right.
$$
$$
\left. \frac{2}{3} \left(\epsilon_{xx} - \epsilon_{\text{hyd}} \right)^2 + \frac{4}{3} \left(\epsilon_{xy}^2 + \epsilon_{xz}^2 + \epsilon_{yz}^2 \right) \right)^{1/2}
$$

(31)

---

[1]The effective strain is the strain equivalent of von Mises stress sometimes referred to as the Mises effective strain.

6. Conclusion

A Bayesian approach to triaxial strain tomography from high-energy X-ray diffraction measurements has been presented. This approach models the strain field as a Gaussian process such that the resulting reconstruction always satisfies equilibrium. From simulated measurements, this method was found to be capable of accurately reconstructing a full strain field in the presence of realistic levels of measurement noise. Through this we have demonstrated that it is possible to tomographically reconstruct a full triaxial strain distribution using single axis tomography. While the squared-exponential covariance function proved suitable in this demonstration, other covariance functions, such as the Matern or rational quadratic, may be more suitable for a particular strain field.

The next stage of this work will involve the planning and execution of an experimental demonstration of the technique. The ability to test the algorithm on simulated strain fields will provide guidance in this process. For example, for a given strain field the trade-off between measurement noise, number of projection angles, and spacing of measurements for each projection can be investigated.

7. Acknowledgements

Appendix A. Approximation Basis Functions

This section provides expressions for the basis functions given in (27) required for the approximation scheme used in Section 4.1.

As stated earlier, a set of bases for the strain field is defined by a linear mapping from a set of bases for the Beltrami stress functions;

$$
\boldsymbol{\phi}_\epsilon(\mathbf{x}_*) = \mathbf{H} \mathcal{B}^{\mathbf{x}} \boldsymbol{\phi}_\Phi(\mathbf{x}_*). \tag{A.1}
$$

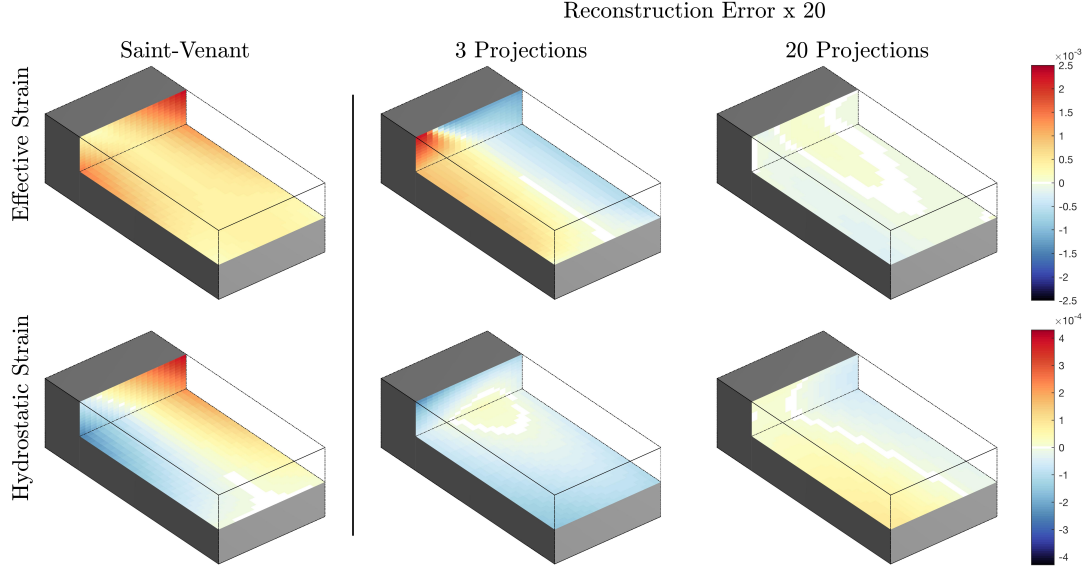This is a linear combination of the partial derivatives of

Figure 5: Shown in 3D is the reconstruction errors for 3 projections (centre) and 20 projections (right) alongside the Saint-Venant strain field (left). The effective strain is shown on the top row and the hydrostatic strain is shown on the bottom row. The magnitude of the error is reduced for 20 projections when compared to the results from 3 projections. The results are shown for two cutting planes; a plane at $z = 0$mm, and a plane at $x = 4$mm.

each Beltrami stress, i, function basis, k;

$$\phi_{i,k} = \frac{1}{\sqrt{L_x L_y L_z}} C_0,$$

$$\frac{\partial^2}{\partial x^2} \phi_{i,k} = \frac{-\lambda_{x,k}^2}{\sqrt{L_x L_y L_z}} C_0,$$

$$\frac{\partial^2}{\partial y^2} \phi_{i,k} = \frac{-\lambda_{y,k}^2}{\sqrt{L_x L_y L_z}} C_0,$$

$$\frac{\partial^2}{\partial z^2} \phi_{i,k} = \frac{-\lambda_{z,k}^2}{\sqrt{L_x L_y L_z}} C_0, \qquad (A.2)$$

$$\frac{\partial^2}{\partial x \partial y} \phi_{i,k} = \frac{\lambda_{x,k} \lambda_{y,k}}{\sqrt{L_x L_y L_z}} C_1,$$

$$\frac{\partial^2}{\partial x \partial z} \phi_{i,k} = \frac{\lambda_{x,k} \lambda_{z,k}}{\sqrt{L_x L_y L_z}} C_2,$$

$$\frac{\partial^2}{\partial y \partial z} \phi_{i,k} = \frac{\lambda_{y,k} \lambda_{z,k}}{\sqrt{L_x L_y L_z}} C_3,$$

where

$$C_0 = \sin\left(\lambda_{x,k}(x + L_x)\right) \sin\left(\lambda_{y,k}(y + L_y)\right) \sin\left(\lambda_{z,k}(z + L_z)\right),$$

$$C_1 = \cos\left(\lambda_{x,k}(x + L_x)\right) \cos\left(\lambda_{y,k}(y + L_y)\right) \sin\left(\lambda_{z,k}(z + L_z)\right),$$

$$C_2 = \cos\left(\lambda_{x,k}(x + L_x)\right) \sin\left(\lambda_{y,k}(y + L_y)\right) \cos\left(\lambda_{z,k}(z + L_z)\right),$$

$$C_3 = \sin\left(\lambda_{x,k}(x + L_x)\right) \cos\left(\lambda_{y,k}(y + L_y)\right) \cos\left(\lambda_{z,k}(z + L_z)\right). \qquad (A.3)$$

Applying the measurement mapping, $\mathcal{L}(eta_i)$ to the basis functions for the strain field gives a set of basis functions for the ith measurement;

$$\boldsymbol{\phi}_{I,i}(\boldsymbol{\eta}_i) = \mathcal{L}^{\mathbf{x}}(\boldsymbol{\eta}_i) \boldsymbol{\phi}_\epsilon(\mathbf{p}_i + \hat{\mathbf{n}}s). \qquad (A.4)$$

Which is a linear combination of the line integrals of the partial derivatives of each basis function. Defining

$$\alpha_x = \lambda_{x,k}(L_x + \hat{n}_1 s + x_0),$$
$$\alpha_y = \lambda_{y,k}(L_y + \hat{n}_2 s + y_0),$$
$$\alpha_z = \lambda_{z,k}(L_z + \hat{n}_3 s + z_0),$$

$$\Gamma_1 = \frac{\cos\left(\alpha_x - \alpha_y - \alpha_z\right)}{\lambda_{x,k} \hat{n}_1 - \lambda_{y,k} \hat{n}_2 - \lambda_{z,k} \hat{n}_3},$$

$$\Gamma_2 = \frac{\cos\left(\alpha_x + \alpha_y - \alpha_z\right)}{\lambda_{x,k} \hat{n}_1 + \lambda_{y,k} \hat{n}_2 - \lambda_{z,k} \hat{n}_3}, \qquad (A.5)$$

$$\Gamma_3 = \frac{\cos\left(\alpha_x - \alpha_y + \alpha_z\right)}{\lambda_{x,k} \hat{n}_1 - \lambda_{y,k} \hat{n}_2 + \lambda_{z,k} \hat{n}_3},$$

$$\Gamma_4 = \frac{\cos\left(\alpha_x + \alpha_y + \alpha_z\right)}{\lambda_{x,k} \hat{n}_1 + \lambda_{y,k} \hat{n}_2 + \lambda_{z,k} \hat{n}_3},$$

the necessary components can be written as

$$\int_0^L \frac{\partial^2 \phi_{i,k}(\mathbf{p}_i + \hat{\mathbf{n}}s)}{\partial x^2}\, ds = \frac{-\lambda_{x,k}^2}{4\sqrt{L_x L_y L_z}}\left(\Gamma_1 - \Gamma_2 - \Gamma_3 + \Gamma_4\right),$$

$$\int_0^L \frac{\partial^2 \phi_{i,k}(\mathbf{p}_i + \hat{\mathbf{n}}s)}{\partial y^2}\, ds = \frac{-\lambda_{y,k}^2}{4\sqrt{L_x L_y L_z}}\left(\Gamma_1 - \Gamma_2 - \Gamma_3 + \Gamma_4\right),$$

$$\int_0^L \frac{\partial^2 \phi_{i,k}(\mathbf{p}_i + \hat{\mathbf{n}}s)}{\partial z^2}\, ds = \frac{-\lambda_{z,k}^2}{4\sqrt{L_x L_y L_z}}\left(\Gamma_1 - \Gamma_2 - \Gamma_3 + \Gamma_4\right),$$

$$\int_0^L \frac{\partial^2 \phi_{i,k}(\mathbf{p}_i + \hat{\mathbf{n}}s)}{\partial x \partial y}\, ds = \frac{\lambda_{x,k}\lambda_{y,k}}{4\sqrt{L_x L_y L_z}}\left(\Gamma_1 + \Gamma_2 - \Gamma_3 - \Gamma_4\right),$$

$$\int_0^L \frac{\partial^2 \phi_{i,k}(\mathbf{p}_i + \hat{\mathbf{n}}s)}{\partial x \partial z}\, ds = \frac{\lambda_{x,k}\lambda_{z,k}}{4\sqrt{L_x L_y L_z}}\left(\Gamma_1 - \Gamma_2 + \Gamma_3 - \Gamma_4\right),$$

$$\int_0^L \frac{\partial^2 \phi_{i,k}(\mathbf{p}_i + \hat{\mathbf{n}}s)}{\partial y \partial z}\, ds = \frac{\lambda_{y,k}\lambda_{z,k}}{4\sqrt{L_x L_y L_z}}\left(-\Gamma_1 - \Gamma_2 - \Gamma_3 - \Gamma_4\right),$$

$$\tag{A.6}$$

References

References

[1] M Croft, Z Zhong, N Jisrawi, I Zakharchenko, RL Holtz, J Skaritka, T Fast, K Sadananda, M Lakshmipathy, and T Tsakalakos. Strain profiling of fatigue crack overload effects using energy dispersive x-ray diffraction. *International Journal of Fatigue*, 27(10-12):1408–1419, 2005.

[2] Michael E Fitzpatrick and Alain Lodini. *Analysis of residual stress by diffraction using neutron and synchrotron radiation.* CRC Press, 2003.

[3] Viktor Hauk. *Structural and residual stress analysis by non-destructive methods: Evaluation-Application-Assessment.* Elsevier, 1997.

[4] J.N. Hendriks, A.W.T. Gregg, C.M. Wensrich, and A. Wills. Implementation of traction constraints in bragg-edge neutron transmission strain tomography. *arXiv preprint arXiv:1805.09760*, 2018.

[5] JN Hendriks, CM Wensrich, A Wills, V Luzin, and AW T Gregg. Robust inference of two-dimensional strain fields from diffraction-based. *arXiv preprint arXiv:1808.06282*, 2018.

[6] Carl Jidling, Johannes Hendriks, Niklas Wahlstrm, Alexander Gregg, Thomas B. Schn, Christopher Wensrich, and Adrian Wills. Probabilistic modelling and reconstruction of strain. *Nuclear Instruments and Methods in Physics Research Section B: Beam Interactions with Materials and Atoms*, 436:141 – 155, 2018. ISSN 0168-583X. doi: https://doi.org/10.1016/j.nimb.2018.08.051.

[7] Erich H Kisi and Christopher J Howard. *Applications of neutron powder diffraction*, volume 15. Oxford University Press, 2012.

[8] Alexander M Korsunsky, Willem JJ Vorster, Shu Yan Zhang, Daniele Dini, David Latham, Mina Golshan, Jian Liu, Yannis Kyriakoglou, and Michael J Walsh. The principle of strain reconstruction tomography: Determination of quench strain distribution from diffraction measurements. *Acta Materialia*, 54(8):2101–2108, 2006.

[9] Alexander M Korsunsky, Nikolaos Baimpas, Xu Song, Jonathan Belnoue, Felix Hofmann, Brian Abbey, Mengyin Xie, Jerome Andrieux, Thomas Buslaps, and Tee Khin Neo. Strain tomography of polycrystalline zirconia dental prostheses by synchrotron x-ray diffraction. *Acta Materialia*, 59(6):2501–2513, 2011.

[10] Ismail C Noyan and Jerome B Cohen. Determination of strain and stress fields by diffraction methods. In *Residual Stress*, pages 117–163. Springer, 1987.

[11] Carl Edward Rasmussen and Christopher KI Williams. *Gaussian processes for machine learning*, volume 1. MIT press Cambridge, 2006.

[12] Martin H Sadd. *Elasticity: theory, applications, and numerics.* Academic Press, 2009.

[13] Arno Solin and Simo Särkkä. Hilbert space methods for reduced-rank gaussian process regression. *arXiv preprint arXiv:1401.5508*, 2014.

[14] Niklas Wahlström. *Modeling of Magnetic Fields and Extended Objects for Localization Applications.* PhD thesis, Linköping University Electronic Press, 2015.

[15] Philip J Withers, Michael Preuss, PJ Webster, DJ Hughes, and Alexander M Korsunsky. Residual strain measurement by synchrotron diffraction. In *Materials science forum*, volume 404, pages 1–12. Trans Tech Publ, 2002.

[16] Stephen Wright and Jorge Nocedal. Numerical optimization. *Springer Science*, 35(67-68):7, 1999.